



## Design optimization of an heat exchanger using Gaussian process

Robin Campet\*, Pamphile T. Roy, Bénédicte Cuenot, Éléonore Riber,  
Jean-Christophe Jouhaud

CERFACS, 42 Avenue Gaspard Coriolis, 31057 Toulouse cedex 1, France



### ARTICLE INFO

#### Article history:

Received 21 September 2019

Revised 8 December 2019

Accepted 21 December 2019

#### Keywords:

Heat exchanger

Geometrical design

Optimization

LES

Ribbed tube

Turbulent channel flow

### ABSTRACT

The objective of this work is to optimize the internal shape of a single-started helically ribbed heat exchanger. Large Eddy Simulation (LES) is used to simulate the turbulent flow in a wall-resolved periodic channel configuration, heated via a uniform heat flux at the wall. In order to enhance the heat exchange with the flow, the inner surface of the channel features rounded rib. This however increases the pressure loss, and an optimum shape of the rib is to be found. The rib pitch and height as well as rib discontinuities are the geometrical parameters to optimize, allowing a wide variety of inner wall roughness. To limit the number of LES, the optimization procedure is based on a surrogate model constructed from *Gaussian Process Regression* and adaptive resampling with the *Efficient Global Optimization* (EGO) method [1]. The optimization consists in the maximization of the cost function proposed by Webb and Eckert [2], which aims at maximizing the heat transfer efficiency for similar pumping power. Results show that a rib induced swirling motion in the near wall region significantly decreases the heat transfer efficiency, leading to an optimum roughness shape featuring large and multiple discontinuities. Moreover, the efficiency of helically dimpled tubes is also found sensitive to the shape of the transitions between the discontinuous parts of the rib. Smoother transitions lead to lower pressure loss but also to lower heat transfer due to smaller recirculation zones.

© 2019 Elsevier Ltd. All rights reserved.

### 1. Introduction

Artificially increasing the roughness of heat exchanger inner surfaces is a passive and efficient method to improve the heat transfer efficiency, and has led to numerous internal designs. The choice of a specific roughness design depends on the flow regime, the fluid properties and also on the device target application. However, roughness always induces an increase in pressure loss which may be detrimental to the system performance and should be limited in that case.

To identify the best design, numerous experimental studies have investigated various turbulence promoter geometries, such as transverse ribs [3,4] or helical ribs [5–8]. More complex three-dimensional geometries were also investigated such as dimpled tubes [9]. Garcia et al. [10] compared the behaviour of corrugated tubes, dimpled tubes and wire coils, concluding to a larger impact of the internal geometry on the pressure drop than on the heat transfer. They also highlighted that better efficiencies are reached with helically corrugated and dimpled tubes for Reynolds numbers greater than 2000, which are geometries comparable to helically

continuous and discontinuous ribbed tubes respectively. Based on those studies, empirical correlations for the prediction of friction and heat transfer efficiency in roughened heat exchangers were derived and can be found in the literature [6,7,9,11–16]. In particular, correlations for simple, 2D roughness geometries such as transverse ribs or helical ribs predict quite accurately the heat exchanger efficiency in a specific range of operating conditions and fluid properties. However, such fitted empirical correlations cannot be extrapolated to other heat exchanger designs for different industrial applications, in particular when considering complex 3D roughness shapes such as helically discontinuous ribs.

In this context, numerical simulation of roughened heated tubes is an attractive alternative for the investigation of heat exchanger efficiencies. Reynolds-Averaged Navier-Stokes (RANS) simulations have been heavily used for this purpose, and various simulations of ribbed tubes can be found in the literature [17–30]. Recently, Large Eddy Simulations (LES) have been introduced for the simulation of ribbed heat exchangers [31–35]. Being more predictive than RANS, LES appears as a more reliable tool for the investigation of pressure loss and heat transfer in a turbulent heat exchanger.

Because of the wide variety of possible roughness shapes, all geometries cannot be experimentally or numerically tested and optimum roughness shapes for heat exchangers remain unknown to

\* Corresponding author.

E-mail address: [robin.campet@gmail.com](mailto:robin.campet@gmail.com) (R. Campet).

## Nomenclature

CDF	Cumulative Density Function
EGO	Efficient Global Optimization
EI	Expected Improvement
GEI	Generalized Expected Improvement
GP	Gaussian Process
LES	Large Eddy Simulation
LSR	Long Smooth Rib
Nu	Nusselt number
PC	Polynomial Chaos
PDF	Probability Density Function
Pr	Prandtl number
QoI	Quantity of Interest
RANS	Reynolds Averaged Navier-Stokes
Re	Reynolds number
SA	Sensitivity Analysis
SSR	Small Smooth Rib
St	Stanton number
A	Exchange surface area
$C_p$	Heat capacity at constant pressure
D	Tube diameter
e	Rib height
E	Total energy
$E_r$	Emptiness ratio
f	Friction factor
$F_{cost}$	Cost function
G	Mass flow per unit area
h	Heat transfer coefficient
k	Covariance function
K	Heat conductance
L	Axial length
$N_D$	Number of discontinuities
$N_{max}$	Maximum number of sample
$n_p$	Dimension of the input sets of variables
$N_s$	Size of the initial sample
$n_x$	Axial component of the wall-normal vector
p	Rib pitch
P	Pressure
$P_p$	Pumping power
R	Tube radius
$r^+$	Normalized radial coordinate
s	Standard error of a distribution
$S_e$	Energy source term
$S_i$	First order Sobol' index
$S_{ij}$	Second order Sobol' index
$S_{qdm}$	Momentum source term
$T_b$	Bulk temperature
$U_b$	Bulk velocity
$u_r$	Radial component of the velocity
$u_x$	Axial component of the velocity
$u_\tau$	Friction velocity
$u_\theta$	Azimuthal component of the velocity
V	Volume of the computational domain
w	Rib floor width
X	Axial distance
$X^+$	Normalized axial distance
y	Wall distance
$y^+$	Dimensionless wall distance
$\lambda$	Fluid thermal conductivity
$\mu$	Mean of a distribution
$\nu$	Fluid kinematic viscosity
$\Omega$	Surface of the computational domain
$\phi$	Probability density function

$\Phi$	Cumulative density function
$\Phi_w$	Heat imposed at the wall
$\rho$	Fluid density
$\tau$	Viscous stress tensor
$\tau_c$	Convective time
$\tau_x$	Axial component of the stress vector
$\mathbf{q}$	Heat flux vector
$\mathbf{S}$	Vector of volumique production source terms
$\mathbf{V}$	Vector of velocity components
$\mathbf{x}$	Sets of input variables
$\mathbf{x}^*$	Specific set of input variables
$\Phi$	Navier-Stokes vector of parameters
$\mathcal{M}$	Surrogate model

date. In this paper a mathematical approach is proposed to determine the optimum roughness shape for industrial heat exchangers. Series of LES are combined to Gaussian Process regression [36] to construct a reliable surrogate model representative of the heat exchanger efficiency for various roughness shapes. This surrogate model is then used to feed the optimisation algorithm, with cost function targeting maximum heat transfer with minimum pressure loss. To the author's knowledge, this work constitutes the first attempt to combine LES with an optimization algorithm for ribbed tubes, and leads to innovative designs for heat exchangers applications. The analysis of the optimum design provides a better understanding of the roughness influence on both pressure drop and heat transfer in ribbed tubes.

The paper is tailored as follows. Section 2 starts with a presentation of the numerical methodology used for the simulation of turbulent heated flow inside various internally ribbed heat exchanger. In particular, the tube inner surface geometry, the meshing method, the governing equations and the objective function to optimize are presented. Sections 3 and 4 then describe the techniques employed to construct the surrogate model as well as its error assessment. After this methodological presentation, Section 5 presents the results of the optimization procedure leading to an optimum discontinuously ribbed tube geometry, makes a detailed analysis of the flow dynamics and thermal behaviour. Section 6 investigates the influence of the rib shape on pressure loss and heat transfer. Smoother shapes representative of dimpled tube geometries are simulated and compared to the optimum geometry studied in Section 5. Finally, Section 7 of this work summarizes the contribution and proposes potential directions for future works.

## 2. Large eddy simulation of ribbed tubes

### 2.1. Geometry and mesh

Simulated heat exchangers are tubular geometries, with a single-started helical rib added on the inner surface inducing artificial roughness for heat transfer enhancement (Fig. 1). For comparison purpose, all tubes have an identical diameter  $D = 38.1$  mm. The rib has a rounded shape, illustrated in Fig. 2, with a floor width  $w$  equal to 3.2864 times the rib height  $e$ . The rib cross-section is then fully characterized only by its height  $e$ . In addition to  $e$ , an important geometrical parameter for the rib shape



Fig. 1. Example of geometry of a helically ribbed tube. 3 pitches of a continuous rib are represented.

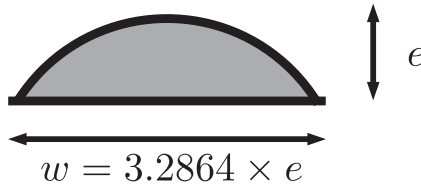


Fig. 2. View of the rounded rib cross-section.

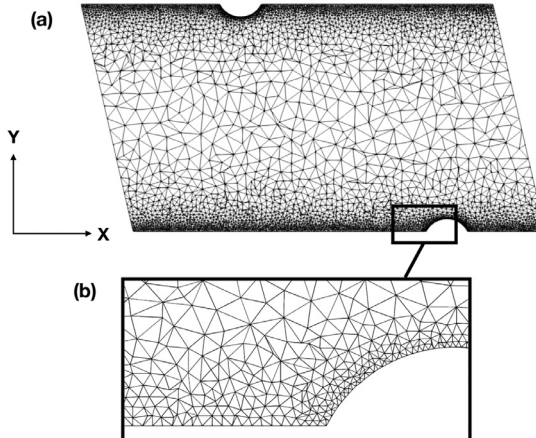


Fig. 3. Example of mesh cut in a central plane for (a) the full computational domain and (b) the detail of the near wall region.

is the rib pitch  $p$ . Both  $e$  and  $p$  are geometrical parameters used for optimization. Note that in this study the pitch-to-height ratio  $p/e$  always remains larger than 8. According to Jimenez and Co-authors [37,38], all ribbed reactor geometries then belong to the K-type roughness ( $p/e > 4$ ) known to greatly affect the bulk flow and enhance heat transfer. As stated by Perry et al. [39], K-type roughness opposes to D-type roughness ( $p/e < 4$ ) for which the ribs are so closely spaced that the eddy shedding from the roughness element has little impact on the bulk flow, which decreases heat transfer. As highlighted by the experimental work of Ravigururajan et al. [13], the shape of the rib cross-section has little influence on the heat transfer enhancement compared to its height and pitch, justifying a constant rounded shape in the current work. Rib discontinuities are also introduced as a geometrical parameter to optimize. Their size and position are fully characterized by the number of discontinuities per rib pitch  $N_D$  and the length of the discontinuity relative to the length of the remaining rib, called the emptiness ratio  $E_r$ .  $N_D$  and  $E_r$  are therefore additional geometrical parameters to optimize, making the total number of input geometrical parameters to optimize equal to 4.

The computational domains consist in one pitch long periodic tubes. Indeed, periodic tubes have been used for long to study turbulent channel flows and proved to give accurate results [40–42], including for helically ribbed tubes [35]. Previous works on helically ribbed tubes using periodic conditions [34,35] showed that the result does not depend on the number of periodic patterns that are computed, as turbulent structures are always found smaller than the rib pitch, even for smaller pitch-to-diameter ratios  $p/D$  than the one studied in the current work. Following the numerical methodology validated by Campet et al. [35] for similar geometries, the meshes are fully unstructured and constituted of tetrahedral cells. Because of the complex flow in the near-wall region due to the presence of the rib, no wall law is applied. The grid is instead sufficiently refined in the near-wall region and in the rib vicinity, as shown in Fig. 3 and a no-slip boundary condition is applied. The influence of the distance to the wall of the first grid

**Table 1**  
Operating conditions common to all simulations.

Flow parameter	Re [-]	$U_b$ [m/s]	$T_b$ [K]	$\nu$ [m <sup>2</sup> /s]	$\Phi_w$ [W/m]
Value	76,800	110	1150	$5.46 \times 10^{-5}$	9576

point on the turbulent flow for this kind of geometry was investigated by Zhu [34], who demonstrated that a dimensionless wall distance  $y^+ = yu_\tau/\nu \approx 10$ , where  $u_\tau$  is the friction velocity and  $\nu$  is the fluid kinematic viscosity, gives good results. Following this recommendation, all simulations are performed with a wall distance of the first grid point away from the wall  $y = 0.323$  mm between two ribs, holding a wall resolution  $y^+ < 20$ , for all simulated geometries. Because of the expected flow acceleration on top of the rib, the cell size is twice smaller on the rib surface to ensure the same resolution criterion. The cell size is then progressively increased toward the centreline to meet LES mesh criteria. Depending on the simulated geometry, resulting meshes contain 2 to 6 million nodes. Other mesh topologies, including fine prism layers on the wall boundaries, were tested on similar configurations by Zhu [34], who concluded to negligible influence on the results given the fine resolution. Each simulation is first run for approximately 50 convective times  $\tau_c = p/U_b$  before collecting flow statistics for approximately 100 convective times  $\tau_c$ . The CPU time of one simulation is about 45,000 h on average and all simulations were computed on 2800 parallel processors, for a corresponding wall-clock-time of about 24 h.

## 2.2. Numerical set-up

The simulations have been performed using the AVBP [43] solver. This parallel code solves the three-dimensional compressible Navier-Stokes equations for both steady and unsteady reacting flows. The Navier-Stokes equations can be written in compact form as:

$$\frac{\partial(\Phi)}{\partial t} + \nabla \cdot (\Phi \mathbf{V}) = \mathbf{S} \quad (1)$$

where  $\mathbf{V}$  is the velocity vector,  $\Phi = [\rho, \rho\mathbf{V}, \rho E]$  with  $\rho$  the density and  $E$  the total energy, and  $\mathbf{S} = [0, -\nabla P + \nabla \cdot \tau, \nabla \cdot (-P\mathbf{V} + \tau \cdot \mathbf{V}) + \nabla \cdot \mathbf{q}]$  with  $\tau$  the viscous stress tensor,  $P$  the pressure and  $\mathbf{q}$  the heat flux is a volumic source term.

The AVBP code is capable of handling hybrid unstructured meshes and allows to address complex geometries. High-order numerical schemes based on the Taylor-Galerkin (TTG) family are used [44] along with the sub-grid scale turbulence model WALE proposed by Nicoud and Ducros [45].

For comparison purposes, all geometries are computed for the same flow regime with the same Reynolds number  $Re = U_b/D/\nu = 76800$ , with  $U_b$  the bulk velocity and  $\nu$  the viscosity of the fluid. Bulk velocity  $U_b$  and bulk temperature  $T_b$  are set constant and similar in all cases, ensuring similar viscosity. Finally, a uniform and constant wall heat flux is imposed at the walls. In order to compare all geometries, they receive the same amount of heat per meter in the axial direction, i.e. the imposed wall heat flux is scaled by the wall inner surface. This amount of heat  $\Phi_w$  is set equal to 9576 W/m, which corresponds to a wall heat flux of 80,000 W/m<sup>2</sup> in a smooth tube of diameter  $D$ . The operating conditions and the fluid properties are representative of thermal cracking processes. They are summarized in Table 1.

In periodic configurations, an artificial source term  $S_{qdm}$  is added to the momentum equation, together with its work counterpart  $u \times S_{qdm}$  in the energy equation, to compensate the pressure loss and ensure a constant flow motion inside the domain.  $S_{qdm}$  is uniformly imposed in the entire domain to avoid artificial pertur-

**Table 2**

Geometrical parameters to optimize and their minimal and maximal considered values.

Geometrical Parameter	Minimal value	Maximal value
$e$ [mm]	0.5	4.5
$p$ [mm]	40	160
$N_D$ [-]	0	5
$E_r$ [-]	0.20	0.80

bations and its value is dynamically adapted to the flow conditions in order to reach the targeted mass flow rate. Similarly, as a heat flux is imposed at the wall, an energy source term  $S_e$  is added to the energy equation, which balances the heat provided to the wall to keep the bulk temperature constant [34].

### 2.3. Optimization problem

All geometrical parameters to optimize are summarized in Table 2, with their minimum and maximum values investigated in this work. Maximum values for  $p$  and  $N_D$  were selected in order to keep the computational cost of the study to a reasonable value, the required simulation time increasing greatly with the increase of those parameters. The allowed range for  $E_r$  is important, as  $E_r = 1$  corresponds to the already extensively studied smooth tube geometry and  $E_r = 0$  reduces to the case of a continuous rib, already investigated with  $N_D = 0$ .

The heat transfer efficiency of a system under forced convection being characterized by the heat transfer coefficient  $h$ , the optimization procedure should lead to a maximization of  $h$  or of the dimensionless Nusselt number  $\text{Nu} = hD/\lambda$ , where  $\lambda$  is the thermal conductivity of the fluid. Similarly, pressure loss in a circular pipe flows are made dimensionless by introducing the friction factor  $f$ , with the following definition:

$$f = \frac{\Delta P D}{2 \rho L U_b^2} \quad (2)$$

where  $\Delta P$  is the global pressure loss in the domain,  $L$  the axial length of the considered geometry,  $\rho$  the fluid density and  $U_b$  the bulk velocity of the flow in the axial direction. Based on those considerations, the cost function to optimize in the context of a single objective optimization study is expected to depend on  $\text{Nu}$  and  $f$ .

Webb and Eckert [2] proposed an estimation of heat exchanger performances, based on the comparison between the heat conductance  $K$ , which is the thermal power provided to the fluid, and the pumping power  $P_p$  required to ensure the motion of the flow. In their work, they focus on the use of rough surfaces in order to maximize the heat exchange capacity for similar pressure drop and exchange surface, or to minimize the pressure drop given the heat exchange capacity and the exchange surface. The heat conductance of the tube is given by  $K = hA$ , with  $A$  the exchange surface. If reported to smooth tube values (with subscript  $s$ ),  $K$  may be also expressed as:

$$\frac{K}{K_s} = \frac{\text{St}}{\text{St}_s} \times \frac{A}{A_s} \times \frac{G}{G_s} \quad (3)$$

with  $\text{St} = h/(U_b \rho C_p)$  the Stanton number and  $G$  the mass flow per unit area. Similarly, the pumping power  $P_p$  can be expressed as a function of the mass flow  $G$ :

$$P_p = \frac{G}{\rho} \times S \times \Delta P \quad (4)$$

Considering the global friction factor defined in Eq. (2), the pumping power becomes:

$$\frac{P_p}{P_{ps}} = \frac{f}{f_s} \times \frac{A}{A_s} \times \left( \frac{G}{G_s} \right)^3 \quad (5)$$

Finally, by eliminating  $G/G_s$  between Eqs. (3) and (5), Webb and Eckert obtained the following expression containing the heat conductance, the pumping power and the exchange area as functions of the Stanton number and the friction factor:

$$\frac{K/K_s}{(P_p/P_{ps})^{1/3} (A/A_s)^{2/3}} = \frac{\text{St}/\text{St}_s}{(f/f_s)^{1/3}} \quad (6)$$

In the current work, a maximization of the heat conductance  $K/K_s$  is targeted for a given pumping power, i.e.  $P_p/P_{ps} = 1$ . It is important to note that in order to reach similar pumping power, the comparison between the smooth and the roughened tube should be done at different operating conditions. This is archived here considering similar exchange surface, i.e.  $A/A_s = 1$ , but different mass flow rates. The cost function to optimize (maximize) therefore reduces to:

$$F_{\text{cost}} = K/K_s = \frac{\text{St}/\text{St}_s}{(f/f_s)^{1/3}} \quad (7)$$

### 3. Optimization method

When dealing with complex cases, the numerical cost is such that only a limited number of simulations can be performed. However, ensuring the convergence of an optimization requires a minimal number of such evaluations for both deterministic and stochastic methods [46]. In this context, building a surrogate of the simulation setup allows to overcome the computational cost [47]. But its quality is paramount and must be controlled.

#### 3.1. Gaussian process-based surrogate model for optimization

There are numerous methods to construct a surrogate model such as Polynomial Chaos (PC) or Gaussian Process (GP). One of the advantage of GP over PC is that it provides an estimation of the variance along with the prediction. This information is required by the optimizer used in this work. The result is a Gaussian Process-based surrogate model is computationally inexpensive and able to predict the quantity of interest (QoI)  $y^*$  at sample  $\mathbf{x}^*$  not part of the initial training sample  $N_s$ .

Consider  $\mathbf{x}$  as a set of random variables such that  $y = F_{\text{cost}}(\mathbf{x})$  follows a joint Gaussian distribution described by its mean  $\bar{y} = \mu(\mathbf{x})$  and covariance  $k(\mathbf{x}, \mathbf{x}')$  [36].

$$y(\mathbf{x}) \sim \mathcal{GP}(\mu(\mathbf{x}), k(\mathbf{x}, \mathbf{x}')), \text{ with} \quad (8)$$

$$\mu(\mathbf{x}) = \mathbb{E}[y(\mathbf{x})],$$

$$k(\mathbf{x}, \mathbf{x}') = \mathbb{E}[(y(\mathbf{x}) - \mu(\mathbf{x}))(y(\mathbf{x}') - \mu(\mathbf{x}'))]$$

Here the covariance function  $k$  (or kernel) is chosen as a Matérn-3/2

$$k(\mathbf{x}, \mathbf{x}') = \left( 1 + \frac{\sqrt{3}r}{l} \right) \exp \left( -\frac{\sqrt{3}r}{l} \right) \quad (9)$$

where  $r = \|\mathbf{x} - \mathbf{x}'\|$  and  $l$  is a length scale that describes the correlations in the data. The matrix of all covariance functions is noted  $\mathcal{K}$ . Then  $\mathcal{M}$  consists of a regression providing a prediction  $\hat{y}$  for any set of input parameters  $\mathbf{x}^*$ :

$$\hat{y}(\mathbf{x}^*) = \bar{y}(\mathbf{x}^*) = \sum_{i=1}^{N_s} \alpha_i k(\mathbf{x}_i, \mathbf{x}^*) \quad (10)$$

with  $\alpha = \mathcal{K}^{-1}\mathbf{y}$

Starting from an initial guess for  $l$ , the fitting phase of the GP consists in selecting  $l$  so that  $y$  passes through the dataset points. A global optimization with a differential evolution strategy is used to find this hyperparameter. It should be noted that, thanks to this automatic optimization of the hyperparameter of the model, no additional constant or coefficient is required from the user.

A key advantage of this method is its ability to provide a prediction for the variance

$$\mathbb{V}[y(\mathbf{x}_*)] = s^2 = k(\mathbf{x}_*, \mathbf{x}_*) - \mathbf{k}(\mathbf{x}_*)^T \mathcal{K}^{-1} \mathbf{k}(\mathbf{x}_*) \quad (11)$$

This property is at the core of the optimization method used in this work and presented in [Section 3.2](#).

### 3.2. Efficient global optimization

With the surrogate model it is easy to find the minimum of  $y$  in the considered range of  $\mathbf{x}$ . However, the nature of the GP tends to smooth out optima. In this work, the *Efficient Global Optimization* (EGO) method [1] is used to improve iteratively the surrogate model, considering a single objective optimization problem. The EGO method is a Bayesian optimization taking into account the variance of the model. The objective of EGO is to improve the current minimum  $y_{\min}$ . The improvement is computed as:

$$I(\mathbf{x}) \begin{cases} y_{\min} - \hat{y}(\mathbf{x}) & \text{if } \hat{y}(\mathbf{x}) < y_{\min} \\ 0 & \text{otherwise} \end{cases} \quad (12)$$

Using the surrogate model, the prediction is expressed as a random process following a normal distribution expressed as  $y \sim \mathcal{N}(\hat{y}, s^2)$ . The expected improvement (EI) is computed as a tradeoff between the minimum value  $y_{\min}$  and an expected value given by the standard error  $s$  for a given prediction  $\hat{y}$ . It reads:

$$\mathbb{E}[I(\mathbf{x})] = (y_{\min} - \hat{y}) \Phi\left(\frac{y_{\min} - \hat{y}(\mathbf{x})}{s}\right) + s\phi\left(\frac{y_{\min} - \hat{y}(\mathbf{x})}{s}\right) \quad (13)$$

with  $\phi(\cdot)$  and  $\Phi(\cdot)$ , respectively, the Probability Density Function (PDF) and Cumulative Distribution Function (CDF) of the normal distribution. Selecting the point with the highest expected improvement is achieved either: (i) by maximizing the difference between the minimum value and the predicted response; or (ii) by increasing the standard deviation. The first method is said to *exploit* the model while the other seeks to *explore* it. These two methods are here automatically selected. In [48], the *Generalized Expected Improvement* (GEI) is proposed as a way to adjust the degree of *exploration vs exploitation* via a constant  $g$ :  $\mathbb{E}[I^g]$ . The highest  $g$  is, the more exploratory the strategy is. Indeed, the EI strategy of [Eq. \(13\)](#) tends to favour improvement of the current solution rather than considering other regions of the parameters space. However the determination of  $g$  is not straightforward and this GEI approach was not applied in this work.

In this study, the open-source BATMAN tool [49] is used for the optimization process. BATMAN handles all the workflow from the design of experiments, to the creation of the surrogate model using the Gaussian Process method and the optimization via the EGO method. Its workflow is presented in [Algorithm 1](#). From an initial sample of size  $N_s$ , a surrogate model  $\mathcal{M}$  is built. An optimization procedure follows which output is a new sample  $\mathbf{x}_*$  to evaluate. The surrogate is updated and the procedure is repeated until a maximum number of sample  $N_{\max}$  is reached.

---

#### Algorithm 1 Workflow using BATMAN.

**Require:**  $N_{\max}$ ,  $N_s$

- 1: Formulate the surrogate  $\mathcal{M}$  on  $N_s$ ' output
  - 2: **while**  $N_s < N_{\max}$  **do**
  - 3:    $\mathbf{x}_* \leftarrow$  optimization
  - 4:   Compute a new sample at  $\mathbf{x}_*$
  - 5:   Update the surrogate  $\mathcal{M}$
  - 6: **end while**
- 

The BATMAN software was developed in Python and relies on extensively validated libraries dedicated to data analysis such

as Scikit-Learn [50]. BATMAN, originally known as JPOD [51], has been tested and validated for optimization problems using Gaussian Process though many studies, such as the work of Braconnier et al. [52]. The present version of BATMAN is provided with many validated test cases [49], and among the recent use of BATMAN for optimization application, one may cite the work of Roy et al. [53] for airfoil optimization.

### 4. Uncertainty quantification

Sensitivity analysis (SA) aims at finding which random variables of the input parameter space are most important toward a QoI [54]. A standard approach is to use the variance which allows to rank these important parameters [55]. Sobol' [56] method is used here with the sole required hypothesis of input variables' independence. This method uses a functional decomposition of the variance:

$$\mathbb{V}(\hat{y}) = \sum_i^{n_p} \mathbb{V}_i(\hat{y}) + \sum_{i < j}^{n_p} \mathbb{V}_{ij}(\hat{y}) + \dots + \mathbb{V}_{1,2,\dots,n_p}(\hat{y}), \quad (14)$$

introducing conditional variances:

$$\mathbb{V}_i(\hat{y}) = \mathbb{V}[\mathbb{E}(\hat{y}|\mathbf{x}_i)], \quad (15)$$

$$\mathbb{V}_{ij}(\hat{y}) = \mathbb{V}[\mathbb{E}(\hat{y}|\mathbf{x}_i \mathbf{x}_j)] - \mathbb{V}_i(\hat{y}) - \mathbb{V}_j(\hat{y}),$$

with  $n_p$  the dimension of  $\mathbf{x}$ . Sobol' indices are expressed as

$$S_i = \frac{\mathbb{V}_i(\hat{y})}{\mathbb{V}[\hat{y}]} \quad S_{ij} = \frac{\mathbb{V}_{ij}(\hat{y})}{\mathbb{V}[\hat{y}]} \quad (16)$$

$S_i$  corresponds to first order terms which apprise the contribution of the  $i$ th parameter, while  $S_{ij}$  corresponds to second order terms which inform about the correlations between the  $i$ th and the  $j$ th parameters. These expressions may be generalized to higher orders. However, the computational effort to converge such statistics is high and most importantly, their analysis and interpretation are not easy.

Total indices represent the global contribution of the parameters on the QoI's variance and write

$$S_{T_i} = S_i + \sum_j S_{ij} + \sum_{j,k} S_{ijk} + \dots = 1 - \frac{\mathbb{V}[\mathbb{E}(\hat{y}|\mathbf{x}_{-i})]}{\mathbb{V}[\hat{y}]} \quad (17)$$

In this work, Sobol' indices are estimated using Martinez' formulation which provides asymptotic confidence intervals [57].

### 5. Results

#### 5.1. Continuous rib

When considering a continuous rib, i.e.,  $N_D = 0$ , the emptiness ratio parameter  $E_r$  becomes irrelevant and the problem reduces to an optimization of 2 input parameters:  $e$  and  $p$ . The response surface constructed with the Gaussian Process method is shown in [Fig. 4](#). Only 8 simulations, indicated by symbols • in [Fig. 4](#), were necessary. Indeed, the evolution of the cost function with  $e$  and  $p$  does not show complex structures which would require additional simulations.

Two optimum regions for the maximization of the objective function appear on the response surface. A first optimum is found for high  $e$  and low  $p$ , while a second optimal is found for high  $e$  and high  $p$ . Based on this observation, it appears that low  $e$  always lead to a poor efficiency of the heat exchanger and high  $e$  ( $e > 2.0$  mm) should be favoured. Note however that the objective function is always evaluated greater than 1.0, assessing better thermal efficiencies than a simple smooth heat exchanger. In the low-pitch optimal region, it appears that the influence of the rib height is of little importance, the cost function remaining quite

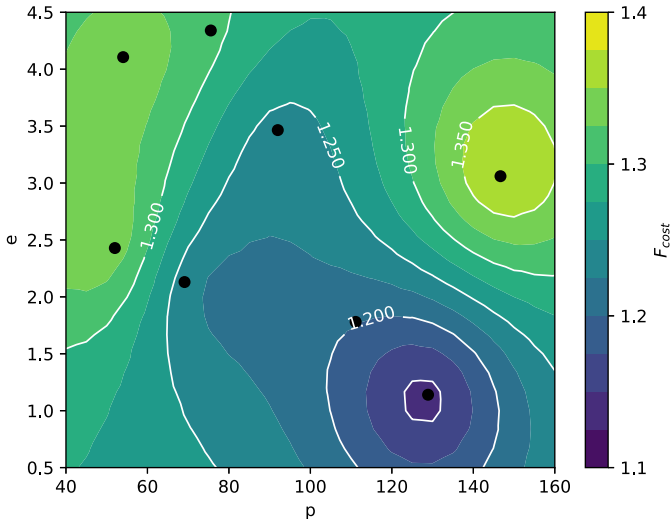


**Fig. 4.** Response surface for a continuous rib.

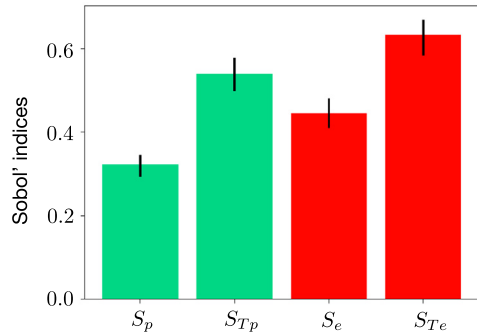


**Fig. 5.** First order and total Sobol' indices for continuous rib optimization.

constant in this zone. Indeed, the combination of small pitch and high height leads to very important pressure loss, which balances the advantage of higher heat transfer efficiency. The high-pitch optimal region seems even more promising than the previous optimal region, the simulation performed in this zone leading to the sample point with maximum cost function. The optimum predicted

value is found to be  $F_{\text{cost}} = 1.374$  for  $e = 3.16 \text{ mm}$  and  $p = 150 \text{ mm}$ . Few observations are done in this zone due to the limited computational cost allocated to the optimization process and more promising reactor design with discontinuous ribs.

**Fig. 5** shows the first order and total Sobol' indices for the two input parameters  $p$  and  $e$ . Both input parameters have an important impact on the response surface,  $e$  impacting slightly more as  $S_p = 0.322$  and  $S_e = 0.444$ . The two parameters are however correlated since the Sobol' total order indices are found significantly higher than the Sobol' first order indices ( $S_{Tp} = 0.538$  and  $S_{Te} = 0.632$ ). Those remarks are consistent with the conclusions drawn from the response surface.

## 5.2. Discontinuous rib

**Fig. 6** shows examples of response surface predicted for ribs with one discontinuity per rib pitch and for different values of  $E_r$ . Thanks to the surrogate model, the total number of simulations performed to cover the parameter space of discontinuous ribs is only 34, to be compared with  $25 \times 25 \times 25 \times 5 = 78125$  that would be required without the surrogate model for the same discretization of the parameter space. The initial design of experiment consisted of 20 simulations and 14 simulations were added thanks to the EGO method.

Results show similarities between the continuous rib response surface given in **Fig. 4** and response surfaces obtained with one small discontinuity ( $N_D = 1$  and  $E_r < 0.5$ ). In both cases maximum values of the cost function are found for large  $e$ , while the minimum values are encountered for small  $e$  and large  $p$ . It should be noted however that for discontinuous ribs with  $E_r < 0.5$ , the region of main interest is found to be the high  $e$  and small  $p$  region, large  $p$  reducing the thermal efficiency of the heat exchanger. On the other hand, a very different response surface is observed for larger discontinuity ( $E_r > 0.6$ ). Intermediate values  $0.5 < E_r < 0.6$  constitute a transition zone between the two behaviours. When the discontinuity becomes larger than the rib itself, the optimum  $p$  value suddenly shifts from 50 mm to about 115 mm. This however has little influence on the optimum rib height, which remains around 4.0 mm. When associated with large  $E_r$ ,  $p$  only modifies the cost function in the  $e > 2.0 \text{ mm}$  region.

Response surfaces obtained for  $N_D$  increasing from 1 to 5 are illustrated in **Fig. 7**. For all investigated numbers of discontinuities, the response of the system to the input parameters is very similar and the observations made for  $N_D = 1$  still hold. In particular,

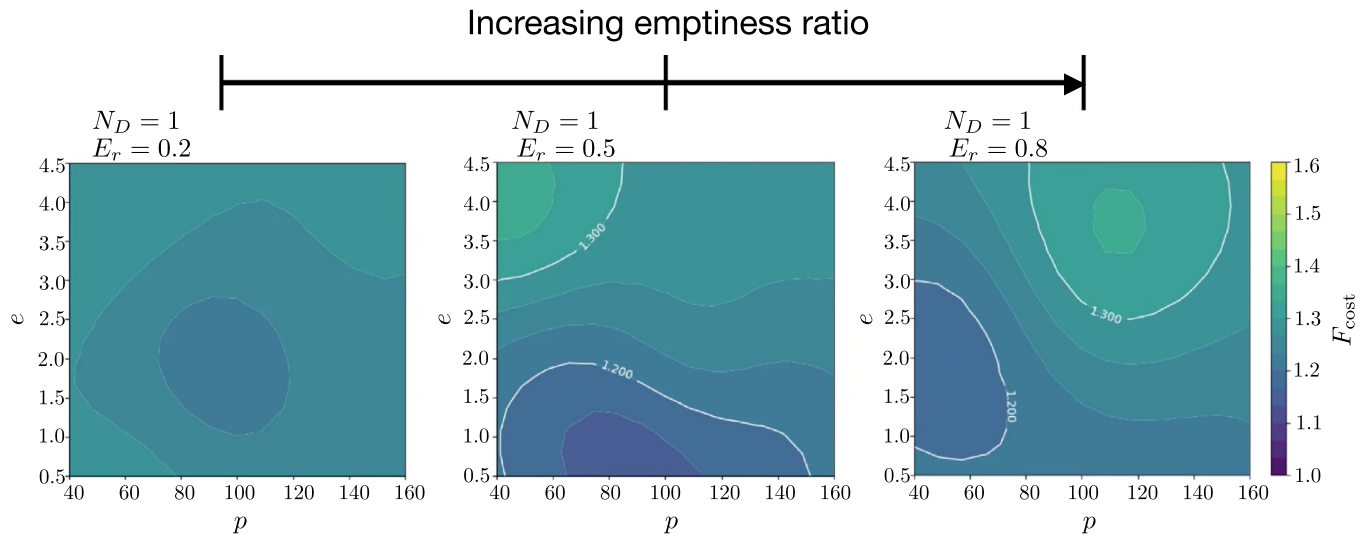


**Fig. 6.** Examples of response surface for a rib with 1 discontinuity per pitch ( $N_D = 1$ ) and various emptiness ratio  $E_r$ .  $E_r = 0.2$  (left),  $E_r = 0.5$  (middle),  $E_r = 0.8$  (right).

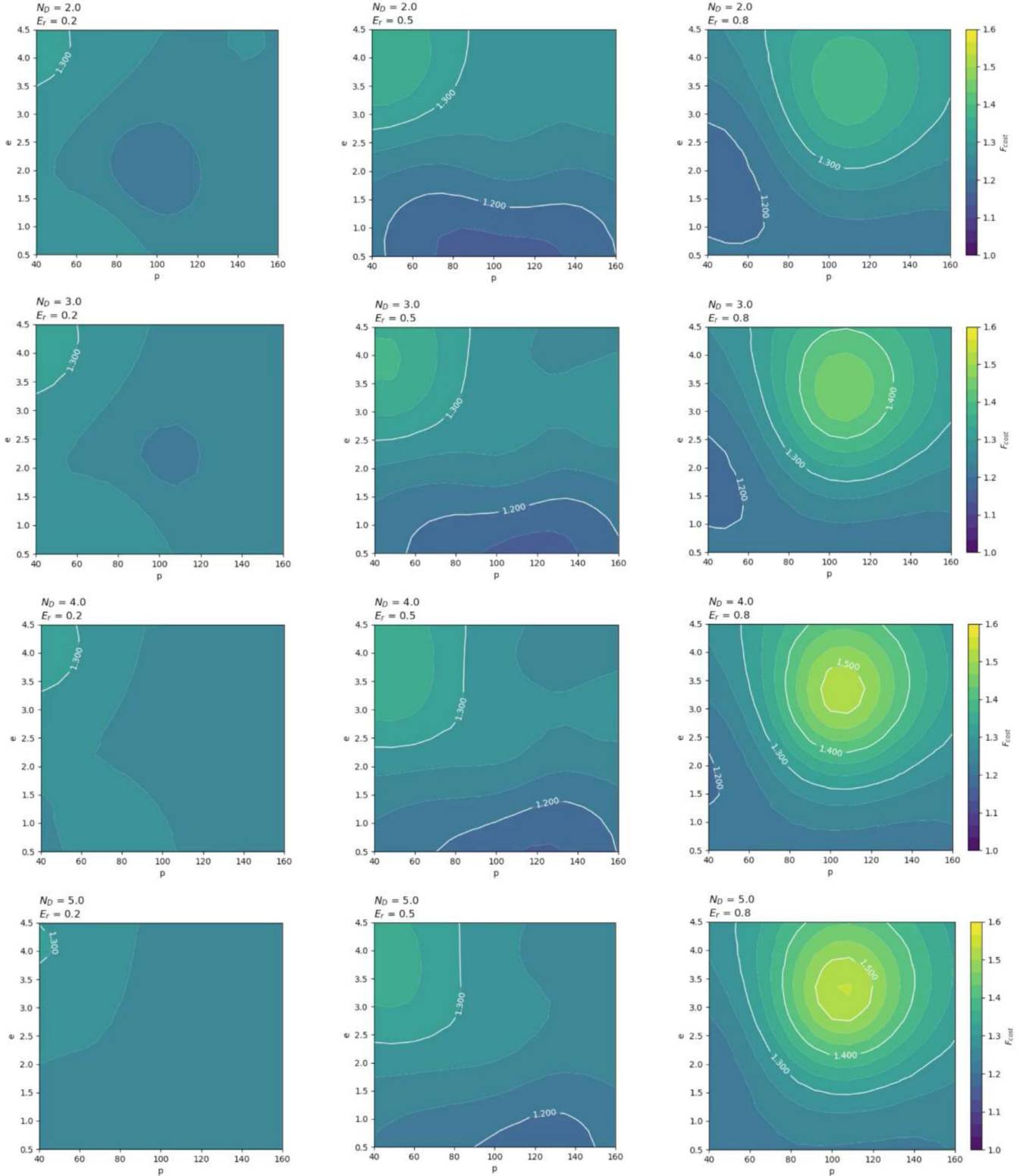
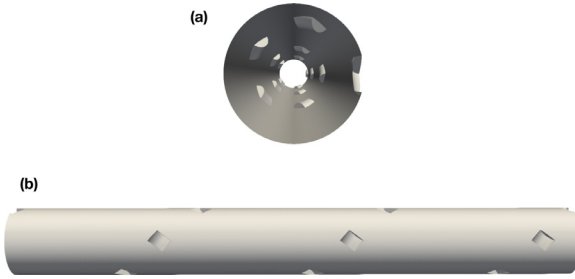


Fig. 7. Examples of response surfaces for various  $N_D$  and  $E_r$ .

the sudden transition in optimum roughness shape is always observed in the same range  $0.5 < E_r < 0.6$ . The main influence of the number of discontinuities is a slight increase of  $F_{cost}$  in the large  $E_r$  region when increasing  $N_D$ , which tends to favour higher number of discontinuities. This is explained by a lower pressure drop while increasing heat transfer enhancements. For  $N_D > 1$ , the

global optimum design that maximizes the cost function clearly appears in the large  $e$ , large  $E_r$  region and for moderate values of  $p$ . Based on these results, the best predicted geometry is shown in Fig. 8, and has the following geometrical parameters:  $e = 3.14$  mm,  $p = 105$  mm,  $E_r = 0.75$  and  $N_D = 5$ . The corresponding value for the cost function is  $F_{cost} = 1.583$ . The dynamic and thermal



**Fig. 8.** Optimum ribbed tube geometry for heat exchanger applications. Three pitches are represented. (a) Cut in the X-normal plane showing the inner surface and (b) view of the wall surface from the outside of the tube.

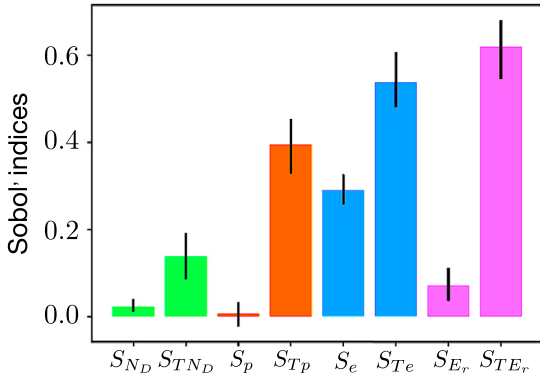


**Fig. 9.** First order and total order Sobol' indices for discontinuous rib optimization.

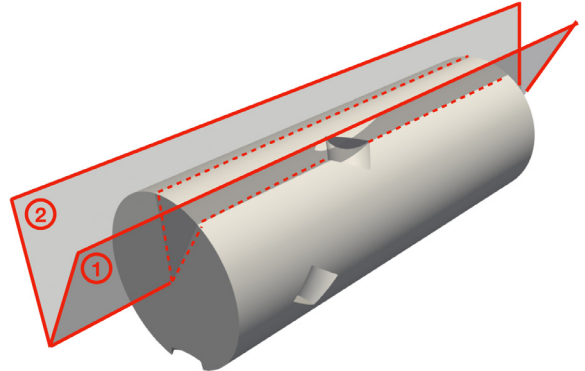
behaviour of the flow in this optimum geometry is described in more details in the next section.

Fig. 9 represents the first and total order Sobol' indices for each input parameter. The rib height  $e$  appears to be of the most influential parameter, the first order Sobol' index reaching a value of  $S_e = 0.290$ . The total order Sobol' index for  $e$  is even higher ( $S_{Te} = 0.539$ ), traducing an influence that depends on the other parameters, and in particular on  $E_r$ . This is consistent with the observed response surfaces, high  $e$  being always more favourable, especially when associated with high values of  $E_r$ . Input parameters  $p$  and  $E_r$  have small first order Sobol' indices ( $S_p = .006$  and  $S_{Er} = 0.070$ ), but their total order indices are much higher ( $S_{Tp} = 0.395$  and  $S_{TEr} = 0.620$ ), meaning non-negligible but complex influence on  $F_{cost}$ . Indeed, the influence of  $p$  appears to be coupled with both  $e$  and  $E_r$ , as small  $e$  and large  $E_r$  always lead to a small impact of  $p$  on the cost function, due to a geometry close to a smooth tube. On the contrary, large values of  $e$  lead to a great impact on the flow, much sensitive to the disposition of the roughness elements, i.e. to  $p$ . Finally,  $N_D$  is the least influential parameter on the cost function. In particular,  $S_{ND} = 0.023$  which is quite small. The total Sobol' index is however not completely negligible ( $S_{TN_D} = 0.138$ ), assessing a small impact of  $N_D$  on the cost function.

### 5.3. Analysis of the optimum discontinuously ribbed heat exchanger

#### 5.3.1. Flow dynamics

Due to the presence of the discontinuous rib, the average flow parameters are functions of both the radial and axial coordinates. The radial coordinate is normalized by the pipe radius  $R$ , ranging from  $r/R = r^+ = 0$  at the pipe centre to  $r^+ = 1$  at the pipe wall. The axial distance  $X$  is normalized by the rib height,  $X/e = X^+ = 0$  being the position of the downstream rib foot at the left periodic plane. Moreover, because of the rib discontinuities, profiles are shown in two different longitudinal planes: the plane cutting the



**Fig. 10.** Representation of the two planes of interest. Plane ① is the longitudinal plane cutting the centre of the rib, and plane ② is the longitudinal plane at the middle of two ribs.

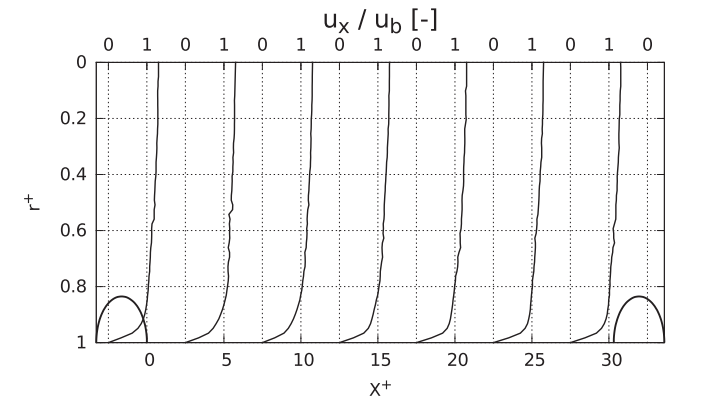
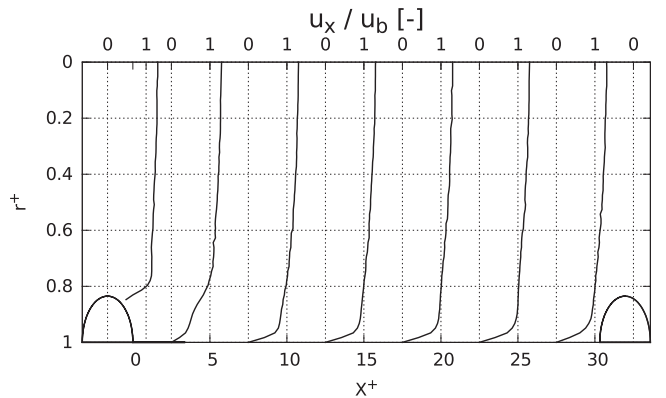


**Fig. 11.** Mean axial normalized velocity profiles at various axial locations, both in plane ① (top) and in plane ② (bottom). Dashed line indicates a rib behind the considered plane.

rib in its centre, called plane ①, and the plane at the middle of two ribs called plane ②, as represented in Fig. 10.

The mean axial velocity profiles normalized by the bulk velocity in plane ① are represented in Fig. 11 (top) for positions  $X^+ = -1$  (rib top), 2.5, 7.5, 12.5, 17.5, 22.5 and 27.5. The mean axial velocity is strongly decelerated in the rib wake. The flow however fully establishes few rib heights farther downstream and all axial velocity profiles are found almost similar between  $X^+ = 7.5$  to  $X^+ = 27.5$ . Because of the rib shape, the recirculation zone is very small and does not appear in Fig. 11, the first represented profile downstream the rib being at position  $X^+ = 2.5$ , i.e., outside the recirculation zone. The recirculation zone actually exhibits a very characteristic 'S' shape due to the rectangular shape of the rib element, including two planes normal to the surface and slantwise to the flow

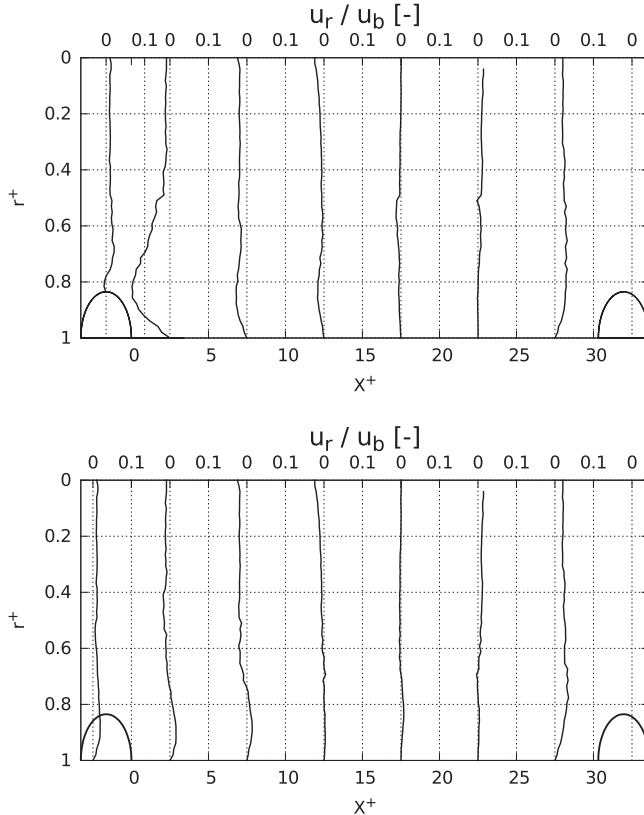


**Fig. 12.** Mean radial normalized velocity profiles at various axial locations, both in plane ① (top) and in plane ② (bottom). Dashed line indicates a rib behind the considered plane.

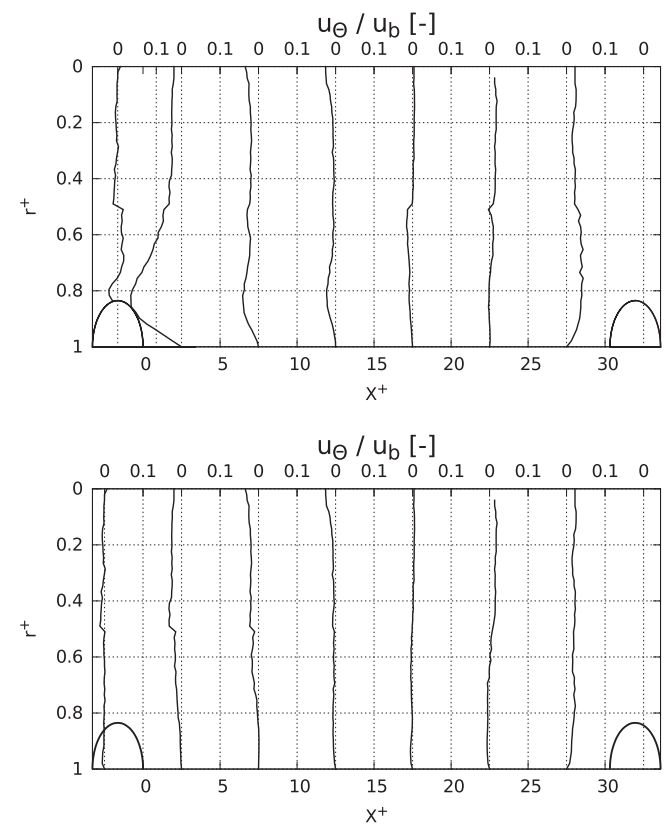


**Fig. 13.** Mean azimuthal normalized velocity profiles at various axial locations, both in plane ① (top) and in plane ② (bottom). Dashed line indicates a rib behind the considered plane.

direction inducing a flow detachment, as represented in Fig. 14. Mean axial velocity profiles in plane ② are also displayed in Fig. 11 (bottom). In the path between two ribs, the axial velocity profiles are similar at all positions, allowing to conclude that the discontinuous rib has no impact on the flow in these zones of the heat exchanger.

The mean radial velocity is investigated in Fig. 12 in both planes ① and ②. It remains very small in plane ②, assessing the low impact of the roughness in this plane. However, a strong negative radial velocity is found in the rib wake, reaching up to  $0.10 \times U_b$ , the mean flow reattaching the wall downstream the recirculation zone. The radial velocity is slightly positive upstream the rib, as the flow goes toward the pipe centre to bypass the obstacle.

Mean azimuthal velocity profiles are displayed in Fig. 13. Similarly to the radial flow motion, the main azimuthal motion is located in the rib wake. Note that at this location, the mean azimuthal velocity is negative, meaning swirling motion in the opposite direction than the rib helix. This is due to the shape of the rib, and in particular to the flow impacting the rib walls oriented perpendicularly to the helix direction. Upstream the rib, a positive mean azimuthal velocity is found in the near wall region, also due to the rib shape orienting the flow. In the rest of the domain, azimuthal motion remains very low, the large space between the ribs preventing the development of a global swirling motion. Indeed, it was observed that the swirling motion disappears for  $E_r > 0.6$ , the rib length shorter than the rib width leading to a different orientation of the flow. This also explains the sudden change in the shape of the cost function when dealing with large  $E_r$ , the swirling motion being detrimental to heat transfer efficiency.

To better visualize the flow, Fig. 15 shows streamlines around the rib. The flow impacting the rib either goes on top or bypasses

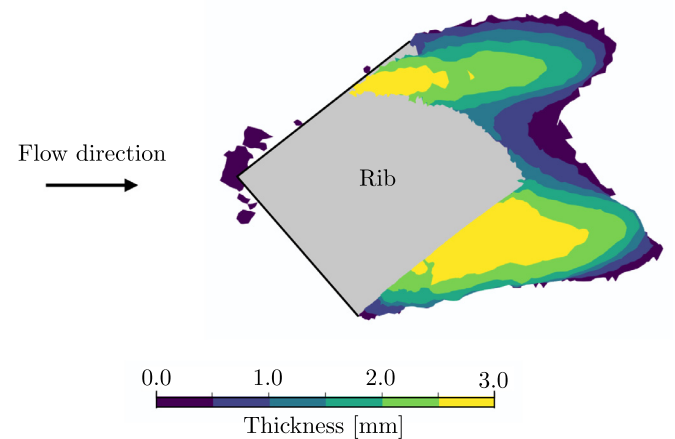


**Fig. 14.** Representation of the mean recirculation zone downstream the rib viewed from above the rib. The iso-surface of zero axial velocity is used to identify the recirculation, and is coloured by the distance of the thickness of the recirculation zone, i.e. the distance of the iso-surface to the tube wall. (For interpretation of the references to colour in this figure legend, the reader is referred to the web version of this article.)

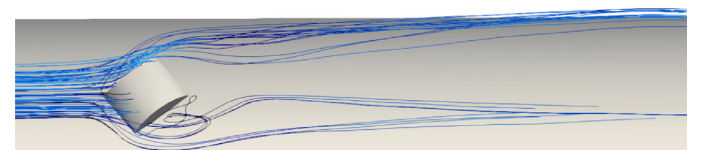


**Fig. 15.** Flow streamlines impacting the rib, coloured by velocity magnitude. (For interpretation of the references to colour in this figure legend, the reader is referred to the web version of this article.)

**Table 3**

Integrated drag contributions normalized by  $(0.5 \rho U_b^2)$  for the optimum geometry and for a smooth tube with the same diameter. Percentages represent the contribution relative to the total drag in a smooth tube according to Eq. (19).

Case	Friction drag ( $\times 10^{-3}$ )	Pressure drag ( $\times 10^{-3}$ )	Total drag ( $\times 10^{-3}$ )
Optimal geometry	3.57 (78.3%)	6.06 (133%)	9.63 (211%)
Smooth tube (Eq. (19))	4.56 (100%)	0 (0%)	4.56 (100%)

**Table 4**

Global pressure loss in the optimum heat exchanger geometry and in a smooth tube according to Eq. (19).

Case	$\Delta P$ [Pa/m]
Optimal geometry	6210
Smooth tube (Eq. (19))	2308

the roughness by both sides, explaining the azimuthal velocity profiles.

The overall dynamics of the tube may be characterized by the time-averaged momentum equation integrated over the domain with periodic conditions:

$$0 = \underbrace{\int_{\Omega} P \vec{n}_x d\vec{S}}_{\text{pressure drag}} + \underbrace{\int_{\Omega} \vec{\tau}_x d\vec{S}}_{\text{friction drag}} + \underbrace{\int_V S_{qdm_x} dV}_{\text{pressure loss}} \quad (18)$$

where  $\Omega$  and  $V$  are respectively the surface and volume of the computational domain, and  $n_x$  and  $\tau_x$  are respectively the axial component of the (inward) wall-normal vector and the axial component of the stress vector.

While in a smooth tube only the friction drag contributes to the pressure loss, in a ribbed tube the pressure loss is due to both the pressure drag and the friction drag. The relative contributions of the pressure drag and the friction drag in the optimum geometry are given in Table 3. It appears that pressure drag is more important than friction drag, due to the flow impacting the rib and the recirculations. Pressure drag is responsible for 63% of the total pressure loss in the optimum geometry. Conversely, the friction drag is lower than in a smooth tube, because of the recirculation zone reducing the axial velocity in the near wall region. Table 4 compares the total pressure loss in the ribbed tube and in a smooth tube of same diameter obtained with the Petukhov correlation [58]:

$$\frac{\partial P}{\partial x} = \frac{1}{(1.58 \ln(\text{Re}) - 3.28)^2} \times \frac{2 \rho U_b^2}{D} \quad (19)$$

Pressure loss is found more than 2 times larger in the ribbed tube.

### 5.3.2. Heat transfer

Wall temperature on the coil inner surface is represented in Fig. 16. It strongly decreases in the recirculation zone and downstream the rib, because of the important radial mixing and the azimuthal motion at this location. This induces large cool zones in the wake of the ribs. The skin temperature is also low on the rib surface, due to the flow acceleration on the rib top inducing important convective heat transfer. On the contrary, because of no swirling motion in the near wall region, the skin temperature is more important between ribs. Quantitative results are given in Fig. 17, showing skin temperature profile in both planes ① and ②. In plane ②, the skin temperature remains approximately constant at 1230 K, as velocity profiles are similar at all axial locations, and

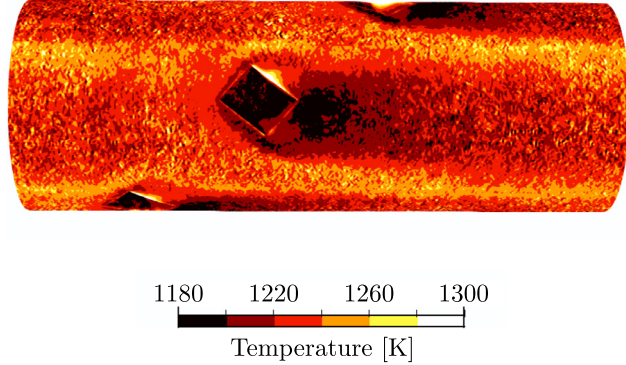


Fig. 16. Mean skin temperature in the optimum geometry.

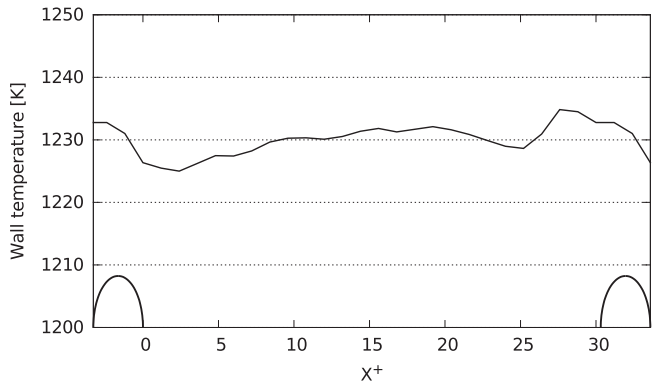
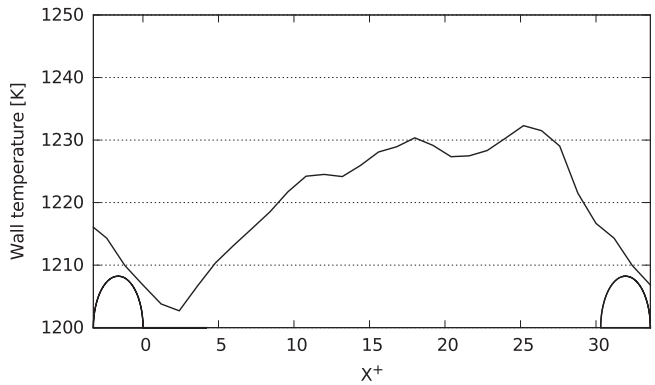
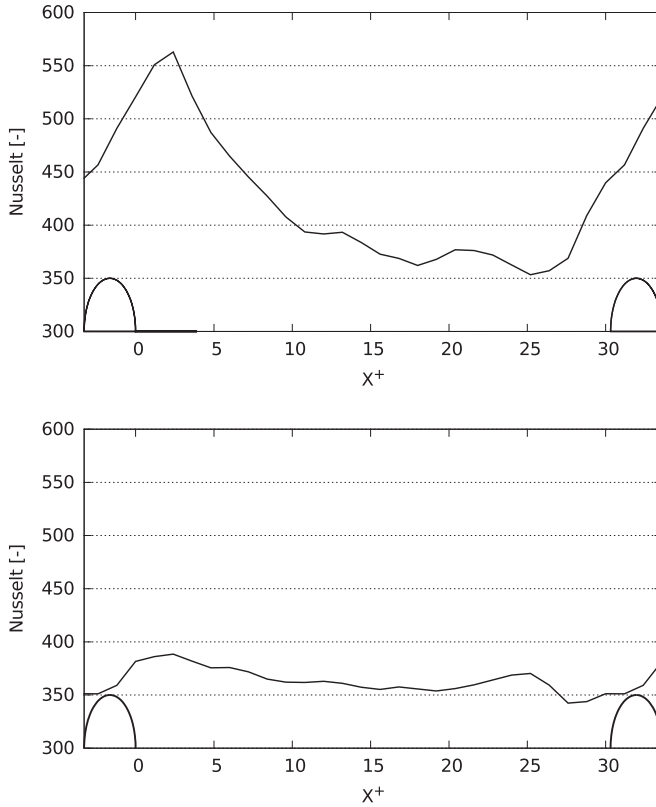


Fig. 17. Profiles of mean skin temperature, in plane ① (top) and in plane ② (bottom). Dashed line indicates a rib behind the considered plane.

no azimuthal mixing occurs. In plane ①, the skin temperature is slightly lower on the rib surface, reaching approximately 1210 K, and decreases to 1203 K in the wake of the rib. It progressively increases downstream until reaching a maximum of 1232 K at location  $X^+ = 25$ .

The global Nusselt number is found equal to 389 in the optimum heat exchanger. In a smooth tube, the Nusselt number evaluated from the Dittus-Boelter correlation [59] (Eq. (20)) is found equal to 189 for the same operating conditions. This represents an increase of + 105% due to both the extended inner tube surface (+2.1%) and to better mixing, leading to an important reduction of the wall temperature. The axial profile of the local Nusselt number is displayed in Fig. 18. In plane ②, the local Nusselt number is approximately constant, which is a consequence of the constant skin temperature. Despite the absence of a rib and swirling motion in this plane, the heat transfer efficiency remains much higher than in a smooth tube, probably due to the cool flow from plane



**Fig. 18.** Profiles of mean local Nusselt number, in plane ① (top) and in plane ② (bottom). Dashed line indicates a rib behind the considered plane.

① impacting the rib and directed toward plane ② from both sides, and to the radial mixing. In plane ① however, the Nusselt number is much higher on the rib surface and in the recirculation zone, reaching a value of 563. This is due to the flow acceleration on the rib top and to the complex recirculation zone enhancing turbulence in the rib wake.

$$\text{Nu}_s = 0.023 \times \text{Re}^{0.8} \times \text{Pr}^{0.4} \quad (20)$$

In the light of these results, reducing the swirl motion in the near wall region of the heat exchanger thanks to large discontinuities seems to increase heat transfer efficiency thanks to an acceleration of the flow on the rib top generating important turbulence intensity in the wake of the rib elements, important radial mixing and an appropriate bending of the flow streamlines in the rib vicinity.

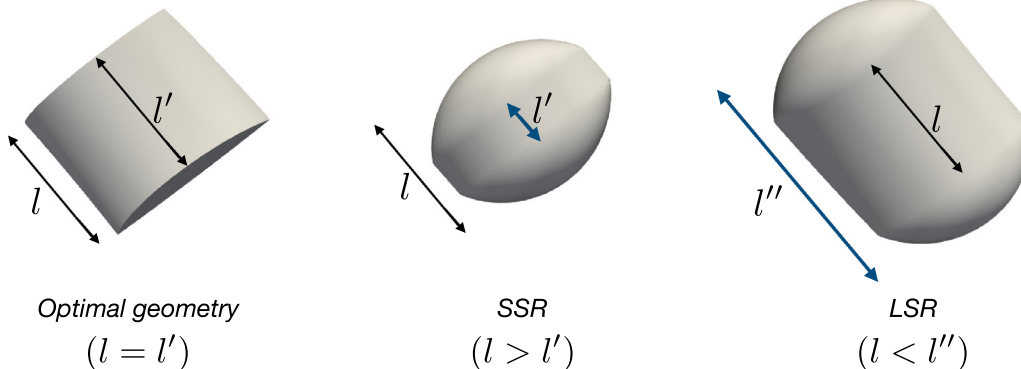


**Fig. 19.** Left: original optimum discontinuous rib shape. Middle: Small Smooth Rib (SSR) shape. Right: Long Smooth Rib (LSR) shape.

## 6. Extension to dimpled heat exchangers

The optimized geometry of the previous section considers rib elements with sharp edges. In real systems however, it is common to use smooth, rounded rib edges. Such systems are called dimpled tubes. In order to evaluate the impact of the rib edge shape, additional simulations of the optimum geometry with smooth rib edges are performed. Because there is no exact equivalence between geometries with sharp and smooth edges, two geometries are simulated: either with the maximum (Long Smooth Rib (LSR)), or with the minimum rib length (Small Smooth Rib (SSR) geometry) equal to the original rib length, as represented in Fig. 19.

### 6.1. Flow dynamics

Mean axial velocity profiles for the three geometries are presented in Fig. 20. It can be seen that in plane ①, all axial velocity profiles are similar except just downstream the rib, at location  $X^+ = 2.5$ . This is due to the different shape of the recirculation zones induced by the different rib shapes. Fig. 24 shows the mean recirculation zones downstream the three different ribs. It appears that the recirculation zone is much reduced with smooth rib edges, and smallest with the LSR shape, where it is limited to the lower part of the rib. As a consequence, the mean axial velocity is highest in the near wall region with the LSR shape and lowest with the original rib, as shown in Fig. 20. In plane ②, the mean axial velocity profiles slightly differ only with the LSR shape in the near wall region, being slightly lower between two ribs ( $X^+ = -2.5$ ) and downstream the rib, up to  $X^+ \approx 5$ , and slightly higher from this position to  $X^+ \approx 22.5$ .

The mean radial and azimuthal velocity profiles are shown in Figs. 21 and 22 respectively. Both in plane ① and ②, azimuthal velocity profiles are very similar between the original rib and the SSR shape, with an almost zero azimuthal velocity everywhere except in the rib vicinity (slightly positive upstream the rib and negative downstream the rib). The only difference lies just downstream the rib, where the azimuthal motion is more important with the original rib shape, which, acting as a larger obstacle, orients more abruptly the flow. The larger LSR shape however induces a stronger mean azimuthal flow in the near wall region, which is strong enough to be seen in plane ②, especially in the rib vicinity. This also impacts the radial motion found more intense with the LSR shape : the flow is driven toward the wall at position  $X^+ = -2.5$ , i.e. between the ribs, and toward the tube centre from position  $X^+ = 12.5$  to  $X^+ = 17.5$ . In plane ①, the radial motion goes in the opposite direction, with a strong radial motion toward the pipe centre on top of the rib and just downstream the rib.

Fig. 23 shows streamlines of the mean flow around the rib for the three considered rib shapes. The difference in flow motion

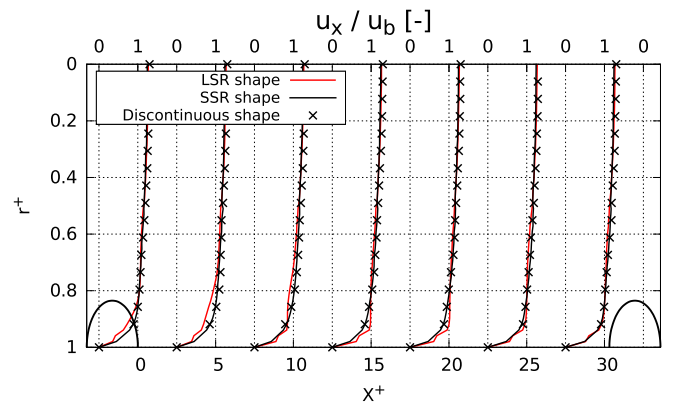
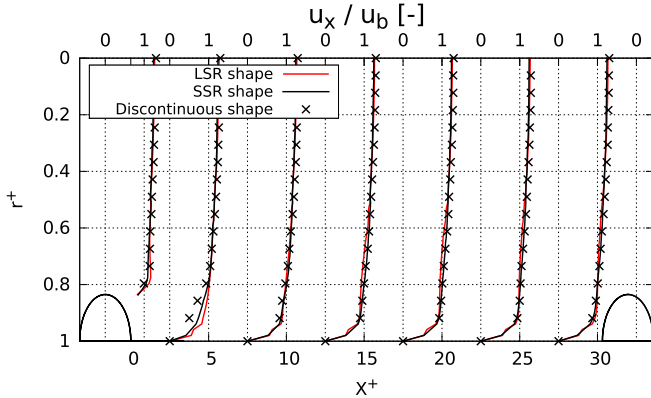


**Fig. 20.** Mean axial normalized velocity profiles in the three studied geometries at various axial locations, in plane ① (top) and in plane ② (bottom). Dashed line indicates a rib behind the considered plane.

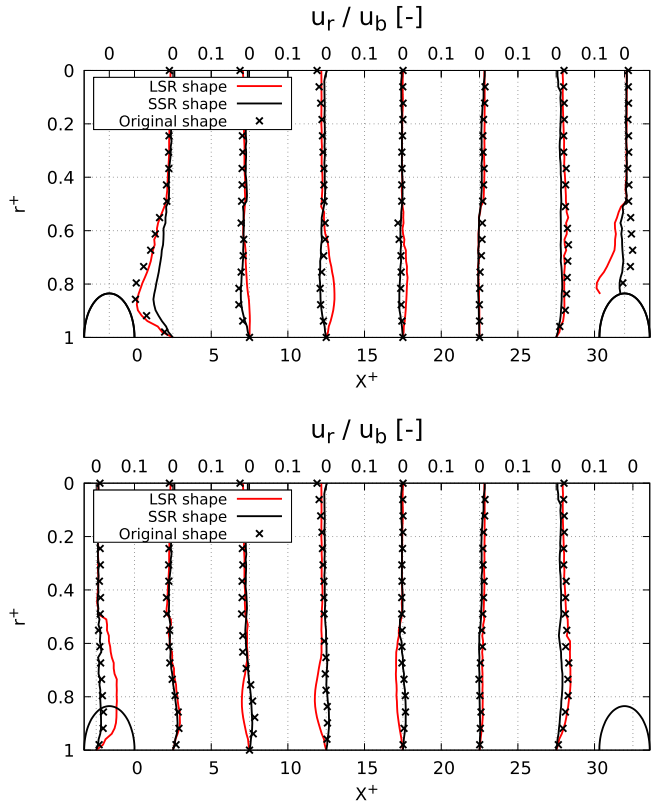


**Fig. 21.** Mean radial normalized velocity profiles in the three studied geometries at various axial locations, in plane ① (top) and in plane ② (bottom). Dashed line indicates a rib behind the considered plane.

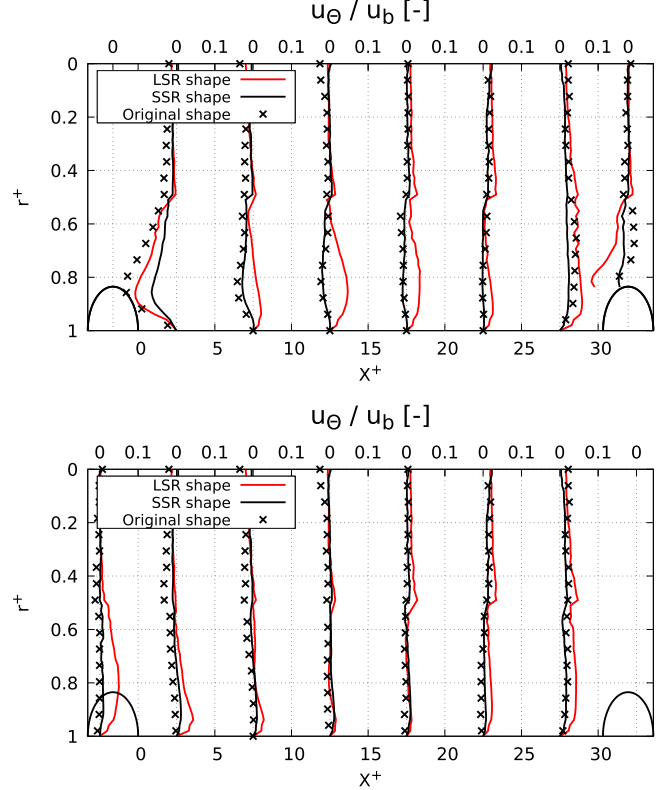


**Fig. 22.** Mean azimuthal normalized velocity profiles in the three studied geometries at various axial locations, in plane ① (top) and in plane ② (bottom). Dashed line indicates a rib behind the considered plane.

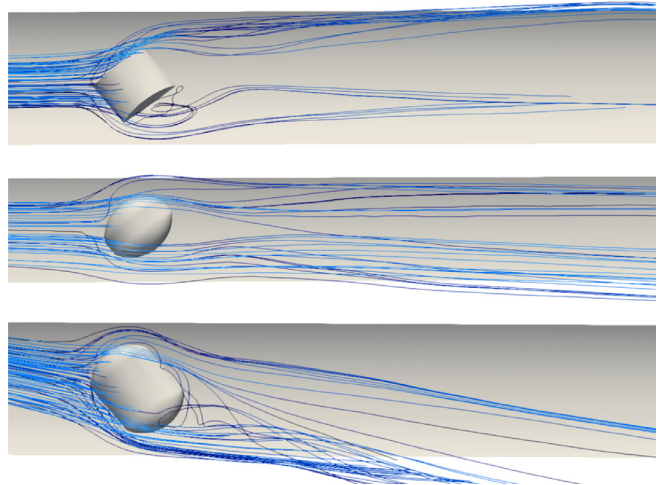


**Fig. 23.** Flow streamlines impacting the rib, coloured by velocity magnitude. Top: optimal discontinuous rib shape. Centre: Small Smooth Rib (SSR) shape. Bottom: Long Smooth Rib (LSR) shape. (For interpretation of the references to colour in this figure legend, the reader is referred to the web version of this article.)

appears very clearly, in particular the more important swirling motion and the smaller recirculation zone found with the LSR shape.

The contributions of pressure and friction to the total drag for both SSR and LSR cases are summarized in Table 5. All ribbed geometries induce similar friction drag, which is reduced by about 25% in comparison with a smooth tube (Eq. (19)). This is due to similar axial velocity profiles encountered in all geometries, leading to similar axial components of wall shear stress. Conversely, the integrated value of the pressure drag is very sensitive to the shape and differs from one geometry to another. Sharp rib edges

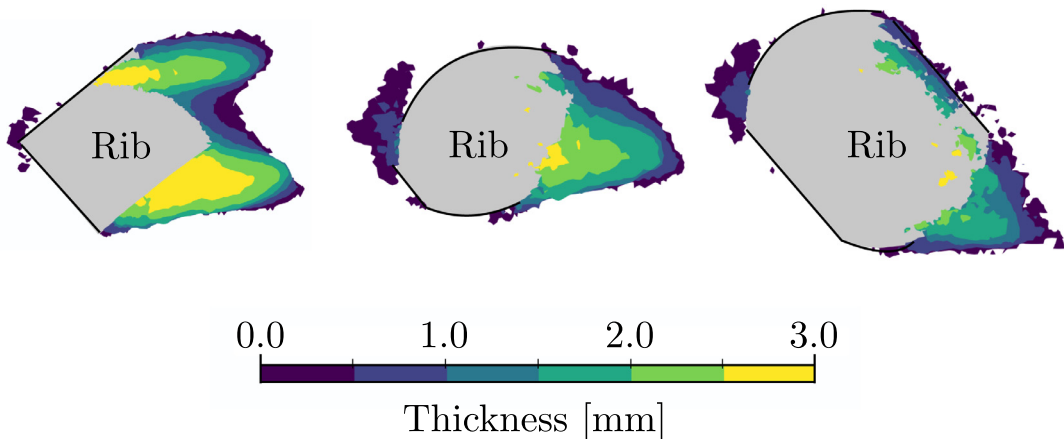


**Fig. 24.** Representation of the mean recirculation zone downstream the ribs, viewed from above the rib. The isosurface of null axial velocity is used as the limits of the recirculation, and is coloured by the thickness of the recirculation zone. Left: optimal discontinuous rib shape. Middle: Small Smooth Rib (SSR) shape. Right: Long Smooth Rib (LSR) shape. (For interpretation of the references to colour in this figure legend, the reader is referred to the web version of this article.)

**Table 5**

Integrated drag contributions normalized by  $(0.5 \rho_b U_b^2)$  for both the SSR and LSR geometries. Percentages represent the contribution relative to the friction drag in a smooth tube estimated from Eq. (19).

Rib shape	Friction drag ( $\times 10^{-3}$ )	Pressure drag ( $\times 10^{-3}$ )	Total drag ( $\times 10^{-3}$ )
SSR	3.36 (73.8%)	2.10 (46.1%)	5.46 (120%)
LSR	3.54 (77.5%)	4.71 (103%)	8.25 (181%)

**Table 6**

Global pressure loss for the three considered rib shapes and for the smooth tube correlation (Eq. (19)).

Case	$\Delta P$ [Pa/m]
Optimal discontinuous rib	6210
SSR	4810
LSR	5720
Smooth tube (Eq. (19))	2308

lead to higher pressure drag, as the flow impacts directly the rib faces, inducing important local pressure gradients. Smoother rib edges reduce significantly the pressure drag, in particular when minimizing the rib surface. With the SSR shape, the pressure drag reduces to less than half the friction drag encountered in a smooth tube (46.1%), and the total drag is only slightly higher than in a smooth tube. The LSR shape leads to slightly lower total drag than the original sharp edges rib. All these observations also hold for the total pressure losses summarized in Table 6.

## 6.2. Impact of the rib shape on heat transfer

Fig. 25 shows the mean wall temperature on the SSR, LSR and the original rib. The temperature distribution is very similar between the original rib and the SSR. In both cases, lower wall temperatures are encountered on the rib top and downstream the rib. Note that due to the smaller recirculation zone in the SSR geometry, the low temperature region downstream the rib is also slightly smaller. In the absence of swirling motion, the flow is slightly hotter in planes between the ribs. With the LSR shape, the swirling motion shifts the coolest zone downstream the rib, elongating them in the azimuthal direction following a helix pattern.

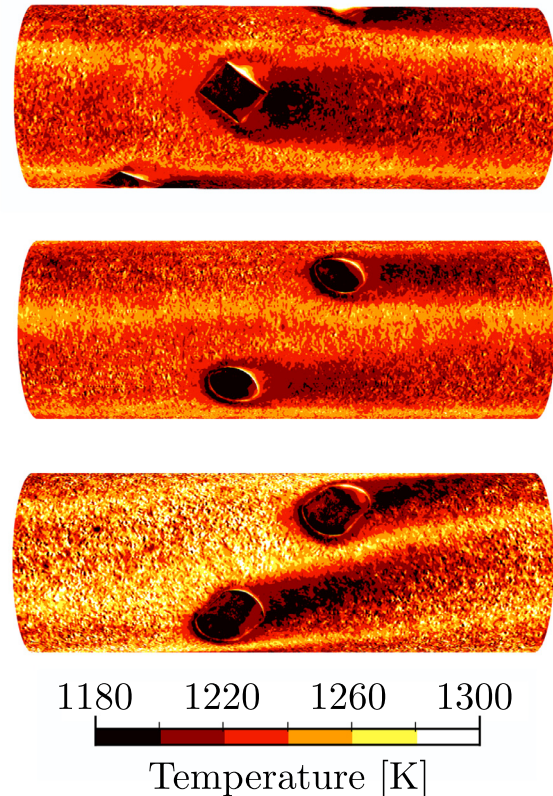


**Fig. 25.** Mean skin temperature for all considered geometries: original rib (top), SSR (middle) and LSR (bottom).

Due to the larger rib size, the flow tends to detach more from the wall, leading to globally lower heat transfer efficiency.

Mean wall temperature profiles in planes ① and ② are shown in Fig. 26. In plane ①, the mean wall temperature is found quite similar between the SSR shape and the original rib shape, whereas with the LSR shape the wall temperature is much higher between the ribs, reaching a maximum value of 1259 K. This is consistent with the observations in Fig. 25 and is due to the local flow detachment around the rib. The mean wall temperature is however found similar for all geometries in the vicinity of the rib. In plane ②, both the SSR and the original rib shapes lead to quasi-constant

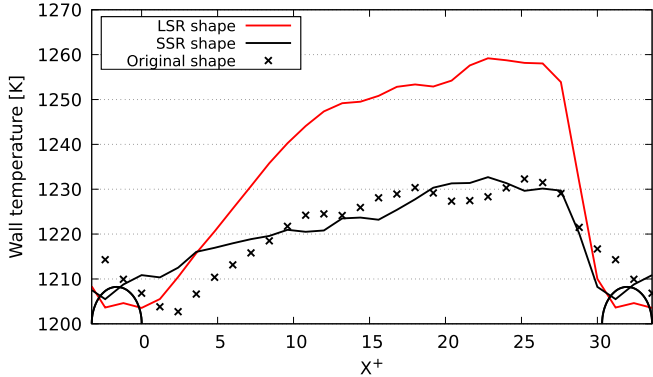


**Fig. 26.** Profiles of mean skin temperature for the three considered geometries, in plane ① (top) and in plane ② (bottom). Dashed line indicates a rib behind the considered plane.

wall temperature, slightly higher with the SSR shape. The LSR shape induces a quite different temperature profile: the swirling motion induces an azimuthal averaging of the flow, and the wall temperature progressively increases from  $X^+ = 10$  to the next rib position ( $X^+ = 28$ ), reaching a value close to the maximum found in plane ① and equal to 1262 K.

Finally, profiles of the local Nusselt number representative of the heat transfer efficiency at the wall are displayed in Fig. 27, both in plane ① and ②. In plane ①, the heat transfer efficiency is similar with the SSR shape and with the original optimum rib shape, resulting in a similar Nusselt number everywhere except immediately downstream the rib and on top of the rib. With the SSR shape, the maximum Nusselt number is found equal to 527 on the rib top. It then progressively decreases, down to the value for the original rib. As previously stated, the heat transfer is lower with the LSR shape, resulting in a lower Nusselt number, except on the top of the rib and in the recirculation zone. In plane ②, the local Nusselt number is found quasi-constant with the SSR shape because of the quasi-constant wall temperature and is slightly lower than with the original rib shape by about 20. The LSR shape leads to a lower Nusselt number from  $X^+ = 15$  to the rib top position consistently with what is observed in plane ①, due to the azimuthal mixing. Integrating the local Nusselt number over the wall surface leads to global Nusselt numbers equal to 354 with the SSR shape, and 332 with the LSR shape. This result assesses a less efficient global heat transfer when using smooth edge ribs when compared to sharp edge ribs of similar size. This is due to the flow being more smoothly directed around the rib, resulting in smaller recirculation zones and lower radial mixing, and a hotter flow downstream the rib. Moreover, it appears that the swirling motion induced by a rib shape such as the LSR shape is detrimental to the heat transfer efficiency, due to the more important blockage ratio

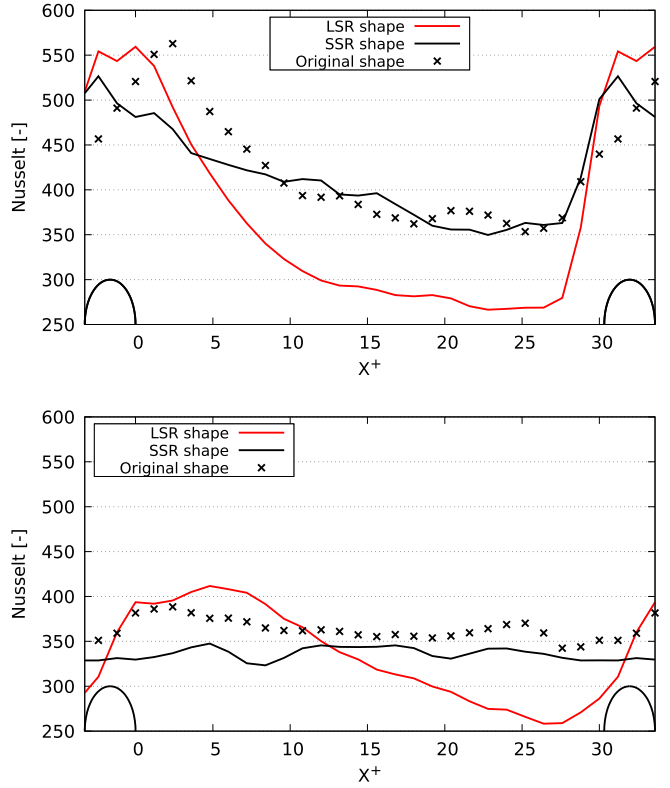


**Fig. 27.** Profiles of mean local Nusselt number for the three considered geometries, in plane ① (top) and in plane ② (bottom). Dashed line indicates a rib behind the considered plane.

leading to a hotter flow in the near wall region, in particular upstream the rib. Thanks to important recirculation zones and to the flow bypassing almost symmetrically the rib, inducing no swirling motion, the original sharp edge shape gives the best heat transfer efficiency.

It should be noted however that much lower pressure loss is obtained with the smooth edge ribs, leading to higher cost functions. In particular, the SSR shape gives  $F_{cost} = 1.628$ , i.e., slightly higher than the sharp edge rib ( $F_{cost} = 1.583$ ). The LSR geometry is less promising ( $F_{cost} = 1.397$ ), mostly because of the poor heat transfer efficiency. The SSR shape may therefore be preferred to the sharp edge rib if pressure loss is critical.

## 7. Conclusions

In this work, a methodology for the simulation and optimization of turbulent flows in heat exchangers has been proposed. It relies on a series of wall resolved LES, using periodic domains. Four geometrical parameters are considered for the optimization, leading to a wide variety of continuous and discontinuous single-started internal roughness geometries. The objective function aims at maximizing the heat transfer efficiency while limiting the pressure loss, as proposed by Webb and Eckert [2]. To avoid running a high number of LES, a surrogate model is built using Gaussian processes. The optimization leads to a heat exchanger geometry which increases the wall heat transfer efficiency by a factor 2.1 compared to a smooth tube, while increasing the pressure loss only by a factor 2.7 for the considered operating conditions, thanks to a roughness with low azimuthal blockage ratio. The introduction of large discontinuities in the rib is responsible for this important increase of heat transfer, because it suppresses the swirling motion, accelerating the flow in the rib vicinity and preserving important radial mixing. Changing the discontinuous rib shape with smoother edges

is found to significantly decrease the pressure loss, but also the heat transfer efficiency in the rib wake, leading to a similar value of the objective function. The investigation of the optimum roughness for heat exchangers might be extended to more geometrical parameters, such as the radius of curvature of the smooth edges for dimpled tubes. The swirling motion being detrimental to the heat transfer efficiency, transverse roughness elements might also be considered instead of helical ones, along with more complex forms.

To summarize, the proposed methodology is found well adapted for geometrical optimization based on few parameters and was successfully applied, leading to innovative geometrical designs for heat exchangers. These heat exchangers may be used for industrial application requiring important heat transfer and limited pressure loss in comparable operating conditions. The optimization methodology may be used in the future with other objective functions for specific industrial applications, such as thermal cracking.

## Declaration of Competing Interest

None.

## CRediT authorship contribution statement

**Robin Campet:** Conceptualization, Methodology, Software, Writing - original draft. **Pamphile T. Roy:** Conceptualization, Methodology, Software. **Bénédicte Cuenot:** Conceptualization, Methodology, Validation, Writing - review & editing. **Éléonore Riber:** Conceptualization, Methodology, Validation, Writing - review & editing. **Jean-Christophe Jouhaud:** Conceptualization, Methodology, Software, Validation, Writing - review & editing.

## Acknowledgments

The financial support provided by all the CERFACS shareholders (AIRBUS, Group, Cnes, EDF, Meteo-France, ONERA, SAFRAN and TOTAL) is greatly appreciated and we thank them for enabling the achievement of such research activities. Furthermore, the authors acknowledge CINES for giving access to HPC resources under the allocation DARI A0032B10157.

## References

- [1] D.R. Jones, M. Schonlau, J. William, Efficient global optimization of expensive black-Box functions, *J. Global Optim.* 13 (4) (1998) 455–492, doi:[10.1023/a:1008306431147](https://doi.org/10.1023/a:1008306431147).
- [2] R.L. Webb, E.R.G. Eckert, Application of rough surfaces to heat exchanger design, *Int. J. Heat Mass Transf.* 15 (9) (1972) 1647–1658.
- [3] R.L. Webb, E.R.G. Eckert, R.J. Goldstein, Heat transfer and friction in tubes with repeated-rib roughness, *Int. J. Heat Mass Transf.* 14 (4) (1971) 601–617.
- [4] D.A. Aliaga, J.P. Lamb, D.E. Klein, Convection heat transfer distributions over plates with square ribs from infrared thermography measurements, *Int. J. Heat Mass Transf.* 37 (3) (1994) 363–374.
- [5] D.L. Gee, R.L. Webb, Forced convection heat transfer in helically rib-roughened tubes, *J. Heat Transf.* 23 (8) (1980) 1127–1136.
- [6] P. Vicente, A. García, A. Viedma, Experimental investigation on heat transfer and frictional characteristics of spirally corrugated tubes in turbulent flow at different prandtl numbers, *Int. J. Heat Mass Transf.* 47 (4) (2004) 671–681.
- [7] L. Cheng, T. Chen, Study of single phase flow heat transfer and friction pressure drop in a spiral internally ribbed tube, *Chem. Eng. Technol.* (2006).
- [8] I. Mayo, B.C. Cernat, M. Virgilio, A. Pappa, T. Arts, Aerothermal investigation on the flow and heat transfer in a helically corrugated cooling channel, in: ASME Turbo Expo 2016: Turbine Technical Conference and Exposition, 2016.
- [9] P.G. Vicente, A. García, A. Viedma, Heat transfer and pressure drop for low Reynolds turbulent flow in helically dimpled tubes, *Int. J. Heat Mass Transf.* 45 (3) (2002) 543–553.
- [10] A. García, J. Solano, P. Vicente, A. Viedma, The influence of artificial roughness shape on heat transfer enhancement: corrugated tubes, dimpled tubes and wire coils, *Appl. Therm. Eng.* 35 (2012) 196–201.
- [11] J. Withers, Tube-side heat transfer and pressure drop for tubes having helical internal ridging with turbulent/transitional flow of single-phase fluid. part 1. single-helix ridging, *Heat Transf. Eng.* 2 (1) (1980) 48–58.
- [12] R. Sethumadhavan, M. Rao, Turbulent flow heat transfer and fluid friction in helical-wire-coil-inserted tubes, *Int. J. Heat Mass Transf.* 26 (12) (1983) 1833–1845.
- [13] T.S. Ravigururajan, A.E. Bergles, Development and verification of general correlations for pressure drop and heat transfer in single-phase turbulent flow in enhanced tubes, *Exp. Therm. Fluid Sci.* 13 (1) (1996) 55–70.
- [14] A. García, P. Vicente, A. Viedma, Experimental study of heat transfer enhancement with wire coil inserts in laminar-transition-turbulent regimes at different prandtl numbers, *Int. J. Heat Mass Transf.* 48 (2005) 4640–4651.
- [15] S. Saha, Thermal and friction characteristics of turbulent flow through rectangular and square ducts with transverse ribs and wire-coil inserts, *Exp. Therm. Fluid Sci.* 34 (2010) 575–589.
- [16] S. Bhattacharyya, S. Saha, Thermohydraulics of laminar flow through a circular tube having integral helical rib roughness and fitted with centre-cleared twisted-tape, *Exp. Therm. Fluid Sci.* 42 (2012) 154–1612.
- [17] T. Liou, J. Hwang, S. Chen, Simulation and measurement of enhanced turbulent heat transfer in a channel with periodic ribs on one principal wall, *Int. J. Heat Mass Transf.* 36 (2) (1993) 507–517.
- [18] L. Shub, Calculation of turbulent flow and heat transfer in a tube with a periodically varying cross-section, *Int. J. Heat Transf.* 36 (4) (1993) 1085–1095.
- [19] X. Liu, M. Jensen, Geometry effects on turbulent flow and heat transfer in internally finned tubes, *J. Heat Transf.* 123 (6) (2001) 1035–1044.
- [20] A. Ooi, G. Iaccarino, P. Durbin, M. Behnia, Reynolds averaged simulation of flow and heat transfer in ribbed ducts, *Int. J. Heat Fluid Flow* 23 (6) (2002) 750–757.
- [21] G. Iaccarino, A. Ooi, P. Durbin, M. Behnia, Conjugate heat transfer predictions in two-dimensional ribbed passages, *Int. J. Heat Fluid Flow* 23 (3) (2002) 340–345.
- [22] T. Liou, S. Chen, K. Shih, Numerical simulation of turbulent flow field and heat transfer in a two-dimensional channel with periodic slit ribs, *Int. J. Heat Mass Transf.* 45 (22) (2002) 4493–4505.
- [23] J. Kim, K. Jansen, M. Jensen, Simulation of three-dimensional incompressible turbulent flow inside tubes with helical fins, *Numer. Heat Transf. Part B* 46 (3) (2004) 195–221.
- [24] H. Kim, K. Kim, Design optimization of rib-roughened channel to enhance turbulent heat transfer, *Int. J. Heat Mass Transf.* 47 (23) (2004) 5159–5168.
- [25] D. Ryu, D. Choi, V. Patel, Analysis of turbulent flow in channels roughened by two-dimensional ribs and three-dimensional blocks. Part i: resistance, *Int. J. Heat Fluid Flow* 28 (5) (2007) 1098–1111.
- [26] D. Ryu, D. Choi, V. Patel, Analysis of turbulent flow in channels roughened by two-dimensional ribs and three-dimensional blocks. Part II: heat transfer, *Int. J. Heat Fluid Flow* 28 (5) (2007) 1112–1124.
- [27] R. Kamali, A. Binesh, The importance of rib shape effects on the local heat transfer and flow friction characteristics of square ducts with ribbed internal surfaces, *Int. Commun. Heat Mass Transf.* 35 (8) (2008) 1032–1040.
- [28] S. Eiamsa-ard, P. Promvonge, Numerical study on heat transfer of turbulent channel flow over periodic grooves, *Int. Commun. Heat Mass Transf.* 35 (7) (2008) 844–852.
- [29] O. Agra, H. Demir, S. Atayilmaz, F. Kantas, A. Dalkilic, Numerical investigation of heat transfer and pressure drop in enhanced tubes, *Int. Commun. Heat Mass Transf.* 38 (10) (2011) 1384–1391.
- [30] T. Ma, Q. Wang, M. Zeng, Y. Chen, Y. Liu, V. Nagarajan, Study on heat transfer and pressure drop performances of ribbed channel in the high temperature heat exchanger, *Appl. Energy* 99 (2012) 393–401.
- [31] S.A. Jordan, The turbulent character and pressure loss produced by periodic symmetric ribs in a circular duct, *Int. J. Heat Fluid Flow* 24 (6) (2003) 795–806.
- [32] S.V. Vijiapurapu, J. Cui, Simulation of turbulent flow in a ribbed pipe using large eddy simulation, *Numer. Heat Transf. Part A* 51 (12) (2007) 1137–1165.
- [33] S. Vijiapurapu, J. Cui, Performance of turbulence models for flows through rough pipes, *Appl. Math. Model.* 34 (6) (2010) 1458–1466.
- [34] M. Zhu, Large Eddy Simulation of Thermal Cracking in Petroleum Industry, Institut National Polytechnique de Toulouse, 2015 Ph.D. thesis. Simulation aux grandes échelles du craquage thermique dans l'industrie pétrochimique
- [35] R. Campet, M. Zhu, E. Riber, B. Cuenot, M. Nemri, Large eddy simulation of a single-started helically ribbed tube with heat transfer, *Int. J. Heat Mass Transf.* 132 (2019) 961–969.
- [36] C. Rasmussen, C. Williams, Gaussian Processes for Machine Learning, MIT Press, 2006.
- [37] J. Jimenez, Turbulent flow over rough walls, *Annu. Rev. Fluid Mech.* 36 (2004) 173–196.
- [38] Y. Nagano, H. Hattori, S.Y. Yasui, T. Houra, DNS of velocity and thermal field in turbulent channel flow with transverse-rib roughness, *Int. J. Heat Fluid Flow* 25 (3) (2004) 393–403.
- [39] A.E. Perry, W.H. Schofield, P.N. Joubert, Rough wall turbulent boundary layers, *J. Fluid Mech.* 37 (2) (1969) 383–413.
- [40] R.S. Rogallo, P. Moin, Numerical simulation of turbulent flows, *Annu. Rev. Fluid Mech.* 16 (1984) 99–137.
- [41] J. Kim, P. Moin, R.D. Moser, Turbulence statistics in fully developed channel flow at low Reynolds number, *J. Fluid Mech.* 177 (1987) 133–166.
- [42] J. Jimenez, P. Moin, The minimal flow unit in near-wall turbulence, *J. Fluid Mech.* 225 (1991) 213–240.
- [43] L. Gicquel, N. Gourdain, J.-F. Boussuge, H. Deniau, G. Staffelbach, P. Wolf, T. Poinsot, High performance parallel computing of flows in complex geometries, *Compt. Rend. Méc.* 339 (2–3) (2011) 104–124.

- [44] L. Quartapelle, V. Selmin, High-order Taylor-Galerkin methods for non-linear multidimensional problems., in: 8th International Conference, Finite Elements in Fluids : New Trends and Applications, 1993.
- [45] F. Nicoud, F. Ducros, Subgrid-scale stress modelling based on the square of the velocity gradient tensor, *Flow Turbul. Combust.* 62 (3) (1999) 183–200.
- [46] M. Cavazzuti, Design of experiments, in: Optimization Methods: From Theory to Design, Springer Berlin Heidelberg, 2013, pp. 13–42, doi:[10.1007/978-3-642-31187-1\\_2](https://doi.org/10.1007/978-3-642-31187-1_2).
- [47] A.I.J. Forrester, A.J. Keane, Recent advances in surrogate-based optimization, *Prog. Aerosp. Sci.* 45 (1–3) (2009) 50–79, doi:[10.1016/j.paerosci.2008.11.001](https://doi.org/10.1016/j.paerosci.2008.11.001).
- [48] M. Schonlau, W.J. Welch, D.R. Jones, Global versus local search in constrained optimization of computer models, in: New Developments and Applications in Experimental Design, 34, 1998, pp. 11–25.
- [49] P.T. Roy, S. Ricci, R. Dupuis, R. Campet, J.-C. Jouhaud, C. Fournier, BATMAN: statistical analysis for expensive computer codes made easy, *J. Open Source Softw.* 3 (21) (2018) 493, doi:[10.21105/joss.00493](https://doi.org/10.21105/joss.00493).
- [50] F. Pedregosa, G. Varoquaux, A. Gramfort, V. Michel, B. Thirion, O. Grisel, M. Blondel, P. Prettenhofer, R. Weiss, V. Dubourg, J. Vanderplas, A. Passos, D. Cournapeau, M. Brucher, M. Perrot, E. Duchesnay, Scikit-learn: machine learning in python, *J. Mach. Learn. Res.* 12 (2011) 2825–2830.
- [51] J.-C. Jouhaud, P. Sagaut, M. Montagnac, J. Laurenceau, A surrogate-Model based multi-disciplinary shape optimization method with application to 2D subsonic airfoil, *Comput. Fluids* 36 (3) (2007) 520–529.
- [52] T. Braconnier, M. Ferrier, J.-C. Jouhaud, M. Montagnac, P. Sagaut, Towards an adaptive POD/SVD surrogate model for aeronautic design, *Comput. Fluids* 40 (1) (2011) 195–209.
- [53] P. Roy, L. Segui, J.-C. Jouhaud, L. Gicquel, Resampling strategies to improve surrogatemodel-based uncertainty quantification - application to LES of LS89, *Int. J. Numer. Methods Fluids* 0 (1) (2018) 1–25.
- [54] B. Iooss, A. Saltelli, Introduction to sensitivity analysis, in: Handbook of Uncertainty Quantification, Springer International Publishing, 2016, pp. 1–20, doi:[10.1007/978-3-319-11259-6\\_31-1](https://doi.org/10.1007/978-3-319-11259-6_31-1).
- [55] F. Ferretti, A. Saltelli, S. Tarantola, Trends in sensitivity analysis practice in the last decade, *Sci. Total Environ.* 568 (2016) 666–670, doi:[10.1016/j.scitotenv.2016.02.133](https://doi.org/10.1016/j.scitotenv.2016.02.133).
- [56] I. Sobol', Sensitivity analysis for nonlinear mathematical models, *Math. Model. Comput. Exp.* 1 (4) (1993) 407–414.
- [57] M. Baudin, K. Boumhaout, T. Delage, B. Iooss, J.-M. Martinez, Numerical stability of Sobol' indices estimation formula, in: 8th International Conference on Sensitivity Analysis of Model Output, Réunion Island, 2016.
- [58] B. Petukhov, V. Popov, Theoretical calculation of heat exchange and frictional resistance in turbulent flow in tubes of an incompressible fluid with variable physical properties, *High Temp. Heat Phys.* 1 (1963) 69–83.
- [59] F. Dittus, L. Boelter, Heat Transfer in automobile radiators of the tubular type, University of California publications in Engineering 2 (1930) 371.